Error Analysis Techniques for Planar Near-Field Measurements

ALLEN C. NEWELL, SENIOR MEMBER, IEEE

Abstract—**The results of an extensive error analysis on planar near-field measurements are described. The analysis provides ways for estimating the magnitude of each individual source of error and then combining them to estimate the total uncertainty in the measurement. Mathematical analysis, computer simulation, and measurement tests are all used where appropriate.**

I. Introduction

FOR ANY measurement technique, a reliable estimate of errors is one of the primary concerns, and this is especially true of a method involving a significant level of mathematical analysis such as the near-field technique. The determination of error bounds for any given antenna/probe/near-field measurement system combination can be a difficult and demanding task, and the mathematical complexity is a major reason for the difficulty. There is often, therefore, a temptation to bypass the mathematics and attempt to establish error bounds for the general measurement technique by a comparison measurement on a specific antenna. In this approach, the results of near-field measurements on a given antenna are compared with far-field measurements, and differences between the two are taken as a measure of the errors in the near-field technique. The limitations of such an approach are as follows. 1) The observed differences are due in part, and perhaps primarily, to errors in the far-field measurement. 2) It is difficult to generalize one result to another antenna or measurement system. 3) There is no indication of which measurement parameters are the most critical or the contribution from each error source. 4) Far-field measurements may be impractical for certain classes of antennas suited to near-field measurements.

This does not mean that comparisons are not valuable. They demonstrate reliability, help to establish confidence without detailed mathematical study, and indicate possible areas where more detailed study should be done. They are one piece in the error analysis puzzle, but certainly not the whole picture.

A complete and general error analysis requires a combination of approaches, both analytical and experimental, to identify all possible error sources and estimate their contribution to final calculated results. Such an analysis provides a tool for the system designer to determine the requirements for each part of a near-field system, and for the metrologist to estimate the uncertainty in measured quantities.

This paper will summarize the results of an extensive error analysis study on planar near-field measurements carried out at the National Bureau of Standards. In some cases, error equations have been derived to predict the effect on far-field quantities such as gain and sidelobe level due to various measurement errors. In other cases, simulation or special tests have been developed to quantify both the near-field error and its effect on results. Examples of some of these tests will be given to illustrate key points in the study.

The comprehensive error analysis is based on a four-part approach. 1) All significant sources of error are identified and itemized. 2) The magnitudes of all near-field error sources are measured or estimated, and in many cases the functional form of the errors can also be determined. This requires, for instance, the use of laser devices to measure the x-, y-, and z-position errors, and calibration techniques to measure receiver linearity. 3) Error equations have been derived or special tests developed to determine the relationship between the near-field measurement errors and the far-field results. 4) The individual error components are correctly combined to give a realistic estimate of the total resultant error.

A. Identifying Error Sources

All possible errors can be divided into three broad categories: theory, numerical calculations, and measurement. Theoretical errors include approximations that are made in the development of the working equations that limit the ultimate accuracy. From a careful study of the theoretical development, we observe that any such errors due to theoretical approximations are either of negligible magnitude or may be considered as measurement errors. For instance, the transmission equation that specifies the measured relative near-field data $B_0'(\mathbf{P})$ and $B_0''(\mathbf{P})$ in terms of the transmitting parameters $\mathbf{t}_{10}(\mathbf{K})$ of the antenna under test (AUT) and the receiving parameters $\mathbf{s}_{02}'(\mathbf{K})$ and $\mathbf{s}_{02}''(\mathbf{K})$ of two independent probes is

$$B_0'(\mathbf{P}) = F' a_0 \int \mathbf{t}_{10}(\mathbf{K}) \cdot \mathbf{s}_{02}'(\mathbf{K}) e^{i\gamma d} e^{i\mathbf{K}\cdot\mathbf{P}}\, d\mathbf{K} \quad (1)$$

$$B_0''(\mathbf{P}) = F'' a_0 \int \mathbf{t}_{10}(\mathbf{K}) \cdot \mathbf{s}_{02}''(\mathbf{K}) e^{i\gamma d} e^{i\mathbf{K}\cdot\mathbf{P}}\, d\mathbf{K}. \quad (2)$$

These relations are derived from Maxwell's equations under the usual assumptions of linearity, single frequency ($e^{-i\omega t}$) operation in free space, and the additional assumption that multiple reflections between the AUT and the probes are negligible. The first assumptions are generally valid to within negligible error, and multiple reflections can be viewed as a measurement error. That is, $B_0'(\mathbf{P})$ and $B_0''(\mathbf{P})$ will be in error due to multiple reflections, but the transmission equation relating error-free near-field data, and error-free probe and

Manuscript received October 1987.
The author is with the Electromagnetic Fields Division, National Bureau of Standards, Boulder, CO 80303.
IEEE Log Number 8821104.

AUT parameters is exact. Similar comments apply to the probe correction relations (7) and (8), and the equations relating conventional far-field quantities to $\mathbf{t}_{10}(\mathbf{k})$. By adopting this point of view, the focus of the error analysis is on the nonideal character of the measurement system, not on the mathematics.

Errors due to numerical calculations arise from roundoff errors in the computer and aliasing errors in the numerical evaluation of the integral in (5) and (6). The roundoff errors for modern computers using at least 32-bit words are much smaller than measurement errors, and they can therefore be neglected. The aliasing errors will be discussed in more detail in the section on measurement errors.

B. Summary of Theory

For later reference, the remaining essential parts of the plane-wave scattering matrix theory are summarized here. In (1) and (2) above, $B_0'(\mathbf{P})$ and $B_0''(\mathbf{P})$ represent the complex output of two probes having nominal orthogonal polarizations, where $\mathbf{P}$ is the x-y position vector on the plane $z = d$. a_0 is the input to the antenna under test. F' and F'' are impedance mismatch factors between the respective probes and the "load" port connected to the probes,

$$F' = \frac{1}{1 - \Gamma_l \Gamma_p'} \qquad F'' = \frac{1}{1 - \Gamma_l \Gamma_p''} \tag{3}$$

where Γ_l, Γ_p', and Γ_p'' are, respectively, the reflection coefficients of the load, the first probe, and the second probe. The transmitting properties of the AUT are specified by the plane-wave transmitting coefficients (PWTC) $\mathbf{t}_{10}(\mathbf{K})$ which are functions of the transverse part of the propagation vector $\mathbf{k}$,

$$\mathbf{K} = k_x \hat{x} + k_y \hat{y} = \mathbf{k} - \gamma \hat{z} \tag{4}$$

where $\gamma = \sqrt{k^2 - K^2}$ denotes the z-component of $\mathbf{k}$. For $e^{-i\omega t}$ time dependence γ is chosen positive real or imaginary. In a similar way, $\mathbf{s}_{02}'(\mathbf{K})$ and $\mathbf{s}_{02}''(\mathbf{K})$ represent the plane-wave receiving coefficients (PWRC) of the two probes. We note that, consistent with the notation employed by Kerns [1] in the original development, the lower case s's and t's represent the *complete* vectors, not merely the transverse x-y components.

The solution for the AUT parameters is accomplished through a Fourier transformation of the measured data followed by a probe correction of the resulting angular spectra $D'(\mathbf{K})$ and $D''(\mathbf{K})$;

$$D'(\mathbf{K}) = \mathbf{t}_{10}(\mathbf{K}) \cdot \mathbf{s}_{02}'(\mathbf{K}) \tag{5a}$$

$$D'(\mathbf{K}) = \frac{e^{-i\gamma d}}{4\pi^2 F' A'} \int B_0'(\mathbf{P}) e^{-i\mathbf{K}\cdot\mathbf{P}}\, d\mathbf{P} \tag{5b}$$

$$D''(\mathbf{K}) = \mathbf{t}_{10}(\mathbf{K}) \cdot \mathbf{s}_{02}''(\mathbf{K}) \tag{6a}$$

$$D''(\mathbf{K}) = \frac{e^{-i\gamma d}}{4\pi^2 F'' A''} \int B_0''(\mathbf{P}) e^{-i\mathbf{K}\cdot\mathbf{P}}\, d\mathbf{P} \tag{6b}$$

$$t_{10m}(\mathbf{K}) = \frac{\dfrac{D'(\mathbf{K})}{s_{02m}'(\mathbf{K})} - \dfrac{D''(\mathbf{K})}{s_{02c}''(\mathbf{K})}\rho_s'(\mathbf{K})}{1 - \rho_s'(\mathbf{K})/\rho_s''(\mathbf{K})} \tag{7}$$

$$t_{10c}(\mathbf{K}) = \frac{\dfrac{D''(\mathbf{K})}{s_{02c}''(\mathbf{K})} - \dfrac{D'(\mathbf{K})}{s_{02m}'(\mathbf{K})\,\rho_s''(\mathbf{K})}}{1 - \rho_s'(\mathbf{K})/\rho_s''(\mathbf{K})}. \tag{8}$$

In these equations, some common conventions have been employed for compactness. The first is to express the ratio $b_0'(\mathbf{P})/a_0$ as the ratio of relative near-field data,

$$B_0'(\mathbf{P}) = \frac{b_0'(\mathbf{P})}{b_0'(\mathbf{P}_0)}, \tag{9}$$

and the normalization constant

$$A' = \frac{a_0}{b_0'(\mathbf{P}_0)}. \tag{10}$$

The near-field amplitude and phase pattern can then be measured relative to the reference point $\mathbf{P}_0$, which is generally at or near the maximum amplitude, and the normalization constant can be measured in a separate procedure. The second convention is the use of m and c subscripts on the plane-wave coefficients in (7) and (8). They are used to denote two orthogonal components of the vectors $\mathbf{t}_{10}(\mathbf{K})$ or $\mathbf{s}_{02}(\mathbf{K})$. They generally denote "main" and "cross" components, however, to be consistent with definitions of polarization ratios (see (14)-(17)), the m subscript specifically denotes either the linear components referred to as elevation, epsilon, vertical, ϕ, or the right-circular component. The c subscript then denotes the corresponding orthogonal components, azimuth, α, horizontal, θ, or left-circular. As a general rule, the probes are chosen such that the first probe couples primarily to the m component and the second one couples primarily to the c component. The probe corresponding to $\mathbf{s}_{02}'(\mathbf{K})$ will therefore be referred to as the m or main-component probe, and the one corresponding to $s_{02}''(\mathbf{K})$ as the c or cross-component probe.

The receiving polarization ratios appearing in (7) and (8) are the ratios of the probe components,

$$\rho_s'(\mathbf{K}) = \frac{s_{02c}'(\mathbf{K})}{s_{02m}'(\mathbf{K})} \tag{11}$$

$$\rho_s''(\mathbf{K}) = \frac{s_{02c}''(\mathbf{K})}{s_{02m}''(\mathbf{K})}. \tag{12}$$

Similar transmitting polarization ratios are defined for the AUT,

$$p_t(\mathbf{K}) = \frac{t_{10c}(\mathbf{K})}{t_{10m}(\mathbf{K})}. \tag{13}$$

The complex polarization ratios are in many ways analogous to transmission-line reflection coefficients, and polarization mismatch factors written in terms of $p_t(\mathbf{K})$ and $\rho_s(\mathbf{K})$ are very similar to impedance mismatch terms. When the coordinate axes coincide with the E-field major axes and the m and c subscripts refer to linear components,

$$\text{tilt angle} = \tau = \pi/2 \text{ or } 0,$$

$$\arg(p_t) = \pi/2,$$

TABLE I
ERROR SOURCES IN PLANAR NEAR-FIELD MEASUREMENTS

Source of Error	Primary Methods of evaluating: Computer Simulation	Test on Measurement System	Error Equations
1) Probe relative pattern			x
2) Probe polarization ratio			x
3) Probe gain measurement			x
4) Probe alignment error			x
5) Normalization constant			x
6) Impedance mismatch factor			x
7) AUT alignment error		x	x
8) Data point spacing (aliasing)		x	x
9) Measurement area truncation	x		x
10) Probe x, y-position errors	x		x
11) Probe z-position errors	x		x
12) Multiple reflections (probe/AUT)		x	
13) Receiver amplitude nonlinearity	x	x	x
14) System phase error due to:		x	x
Receiver phase errors			
Flexing cables/rotary joints			
Temperature effects			
15) Receiver dynamic range		x	
16) Room scattering		x	
17) Leakage and crosstalk		x	x
18) Random errors in amplitude/phase	x	x	x

and

$$\text{axial ratio} = \text{AR} = |p_t|.$$

In the main beam region of linearly polarized antennas, these conditions are often fulfilled, and p_t can therefore be thought of as a complex axial ratio. Familiar polarization parameters such as axial ratio, AR(**K**) and tilt angle $\tau(\mathbf{K})$ then follow from the polarization ratios, but the form of the relations depends upon whether linear or circular components are being denoted by the m and c subscripts. If circular components are being used, m denotes the right-circular component and c the left. In this case,

$$\text{AR}(\mathbf{K}) = \frac{1+|p_t(\mathbf{K})|}{1-|p_t(\mathbf{K})|} \tag{14}$$

and

$$\tau(\mathbf{K}) = 1/2 \arg\,(p_t(\mathbf{K})). \tag{15}$$

If linear components are being used,

$$\text{AR}(\mathbf{K}) = \frac{1+\left|\dfrac{p_t(\mathbf{K})+i}{p_t(\mathbf{K})-i}\right|}{1-\left|\dfrac{p_t(\mathbf{K})+i}{p_t(\mathbf{K})-i}\right|} \tag{16}$$

$$\tau(\mathbf{K}) = 1/2 \arg\left(\frac{p_t(\mathbf{K})+i}{p_t(\mathbf{K})-i}\right). \tag{17}$$

It is important to realize that the plane-wave scattering matrix coefficients are power normalized [1] so that *absolute* quantities such as power gain, receiving area, and far-electric field follow directly from a solution for $\mathbf{t}_{10}(\mathbf{K})$. The defining equations for the basic quantities are

$$G(\mathbf{K}) = \frac{4\pi Y_0 \gamma^2 |\mathbf{t}_{10}(\mathbf{K})|^2}{\eta_0(1-|\Gamma_a|^2)} \tag{18}$$

$$\sigma(\mathbf{K}) = \frac{4\pi^2 \eta_0 |\mathbf{s}'_{02}(\mathbf{K})|^2}{Y_0(1-|\Gamma'_p|^2)} \tag{19}$$

$$\mathbf{E}(\mathbf{r}) \sim \frac{i\gamma}{r}\,\mathbf{t}_{10}(\mathbf{R}k/r)a_0 e^{ikr} \tag{20}$$

where $G(\mathbf{K})$ denotes the power-gain function, $\sigma(\mathbf{K})$ is the receiving effective area, $Y_0 = \sqrt{\epsilon/\mu}$ is the plane-wave admittance in the space medium, η_0 is the characteristic admittance for propagated waves in the transmission line connected to the antennas, Γ_a is the AUT's reflection coefficient, and $\mathbf{r}$ is the position vector with transverse part $\mathbf{R}$,

$$\mathbf{r} = \mathbf{R} + z\mathbf{e}_z. \tag{21}$$

II. Measurement Errors

The errors due to the measurement system are the major source and will be the primary focus of the remaining discussion. We begin by itemizing in Table I the individual error sources. The noted methods for evaluation are described in detail with each source and are the means for quantifying the error effect on far-field results.

The measurement system errors listed in Table I can be considered in two broad categories. The first are uncertainties in probe parameters arising from the gain, polarization, and pattern measurements used to obtain $\mathbf{s}_{02}(\mathbf{K})$, and the second are errors in the calculated spectra $D'(\mathbf{K})$ and $D''(\mathbf{K})$ arising from the measured data $B''_0(\mathbf{P})$, $B''_0(\mathbf{P})$, A', A'', and the various reflection coefficients. Before discussing these errors, some general comments are made. With the exception of error 18,

all of those listed in Table I are primarily systematic. They may have a small random component, but those components are all combined in error 18. Second, most of the error sources produce an "error spectrum." This means, for instance, that the error may vary as a function of x and y in a repeatable and deterministic manner, and under Fourier transform produces an error spectrum. In the case of probe pattern errors, they vary with **K**, and therefore the spectrum is obvious. Finally, each of the errors is assumed independent and uncorrelated with any other error. They can all be treated separately and combined using their independent character.

A. Probe Parameter Errors

The effect of probe errors (items 1–4 in Table I) will be considered first and will depend on the probe's polarization properties relative to those of the AUT. Every case cannot be considered here, but we will consider the most common ones. Others may be derived by similar application of the basic relations. We will assume that the first probe couples primarily to the main component of the AUT; the second responds primarily to the cross component; therefore, the AUT's and probe's polarization ratios satisfy the conditions

$$\left|\frac{s_c'(\mathbf{K})s_m''(\mathbf{K})}{s_m'(\mathbf{K})s_c''(\mathbf{K})}\right| = |\rho_s'(\mathbf{K})/\rho_s''(\mathbf{K})| \ll 1 \tag{22}$$

$$|\rho_s'(\mathbf{K})p_t(\mathbf{K})| < 1 \tag{23}$$

for all values of **K** where results are desired. The 10 and 02 subscripts in these and following equations have been deleted for brevity. The probe correction equations then reduce to

$$t_m(\mathbf{K}) = \frac{D'(\mathbf{K})}{s_m'(\mathbf{K})} \tag{24}$$

$$t_c(\mathbf{K}) - \frac{D''(\mathbf{K})}{s_c''(\mathbf{K})} - \frac{D'(\mathbf{K})}{s_m'(\mathbf{K})\rho_s''(\mathbf{K})}. \tag{25}$$

The fractional errors in each of these components are

$$\frac{dt_m(\mathbf{K})}{t_m(\mathbf{K})} = \frac{dD'(\mathbf{K})}{D'(\mathbf{K})} - \frac{ds_m'(\mathbf{K})}{s_m'(\mathbf{K})} \tag{26}$$

$$\begin{aligned}\frac{dt_c(\mathbf{K})}{t_c(\mathbf{K})} = {} & \left(1 + \frac{1}{p_t(\mathbf{K})\rho_s''(\mathbf{K})}\right) \\ & \cdot \left(\frac{dD''(\mathbf{K})}{D''(\mathbf{K})} - \frac{ds_c''(\mathbf{K})}{s_c''(\mathbf{K})}\right) \\ & + \frac{1}{p_t(\mathbf{K})\rho_s''(\mathbf{K})}\left(\frac{d\rho_s''(\mathbf{K})}{\rho_s''(\mathbf{K})}\right. \\ & \left. - \frac{dD'(\mathbf{K})}{D'(\mathbf{K})} + \frac{ds_m'(\mathbf{K})}{s_m'(\mathbf{K})}\right).\end{aligned} \tag{27}$$

Focusing attention on the terms involving the two probe's parameters, the following conclusions can be drawn. 1) If the polarization ratio of the first probe satisfies the requirements in (22) and (23), uncertainties in $\rho_s'(\mathbf{K})$ have no significant effect on the determination of either component. Under these conditions, the cross-polarized response of the main component probe has no significant effect on the measurement. 2) Since the AUT's main component pattern and partial gain are proportional to $t_m(\mathbf{K})$, the errors in the main component, arising from probe errors are one-to-one. That is, they have the same magnitude as the errors in $s_m'(\mathbf{K})$, and the result in a given direction (specified by **(K)**) is affected by the probe's pattern in that same direction. This is in contrast to the cylindrical and spherical near-field measurements where the result in one direction is affected by the probe's pattern over an extended region. 3) The probe's effect on the AUT cross polarization depends on the relative polarization ratios of the AUT and the second probe.

1) For regions where

$$p_t(\mathbf{K})\rho_s''(\mathbf{K}) \gg 1, \tag{28}$$

(27) reduces to the same form as (26) and errors in t_c are produced only by errors in D'' and s_c''. This condition is likely to exist in the sidelobe region of the AUT where p_t may approach 1, but ρ_s'' is still quite large, as illustrated by Fig. 1. In a sense, when (28) is satisfied, the probe is "better" polarized than the antenna being measured.

2) In the region of the main beam, however, the product of the polarization ratios may approach 1,

$$|p_t(\mathbf{K})\rho_s''(\mathbf{K})| \simeq 1, \tag{29}$$

because the AUT and cross-polarized probe have similar axial ratios but are orthogonally polarized. In that case, all the terms of (27) are significant and errors in ρ_s'', D', and s_m' also produce errors in t_c. In either case, the uncertainties in probe parameters are obtained from a knowledge of the errors in the probe calibration process and then used in (26) and (27).

Another useful form of the error equation for probe effects comes from considering the error in the AUT polarization ratio rather than the individual components. Equations (24) and (25) show that

$$p_{t\epsilon}(\mathbf{K}) = \frac{t_c(\mathbf{K})}{t_m(\mathbf{K})} = \frac{D''(\mathbf{K})s_m'(\mathbf{K})}{D'(\mathbf{K})s_c''(\mathbf{K})} - \frac{1}{\rho_{s\epsilon}''(\mathbf{K})}. \tag{30}$$

An additional ϵ subscript has been added to p_t and the $\rho_s''(\mathbf{K})$ in the second term of (30) since we want to consider the effect of errors in $\rho_s''(\mathbf{K})$ on the AUT polarization results. $\rho_{s\epsilon}''(\mathbf{K})$ represents erroneous values for the cross-polarized probe polarization and $P_{t\epsilon}$, the resulting AUT parameter. The first term in (30) is evaluated using (5a) and (6a), giving

$$p_{t\epsilon}(\mathbf{K}) \simeq p_t(\mathbf{K}) + \frac{1}{\rho_s''(\mathbf{K})} - \frac{1}{\rho_{s\epsilon}''(\mathbf{K})}. \tag{31}$$

The ratio of measured to actual polarization is then

$$\frac{p_{t\epsilon}(\mathbf{K})}{p_t(\mathbf{K})} \simeq 1 + \frac{1}{p_t(\mathbf{K})\rho_s''(\mathbf{K})} - \frac{1}{p_t(\mathbf{K})\rho_{s\epsilon}''(\mathbf{K})}. \tag{32}$$

Four typical cases will illustrate how (32) is used. The first two relate to nominally linearly polarized AUT and probes with the E-field and coordinate axes approximately coincident.

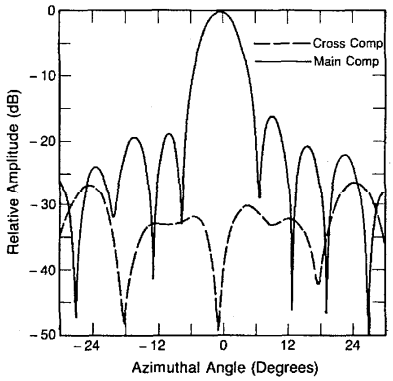

Fig. 1. Typical main and cross component patterns for AUT where magnitudes are approximately same in sidelobe region.

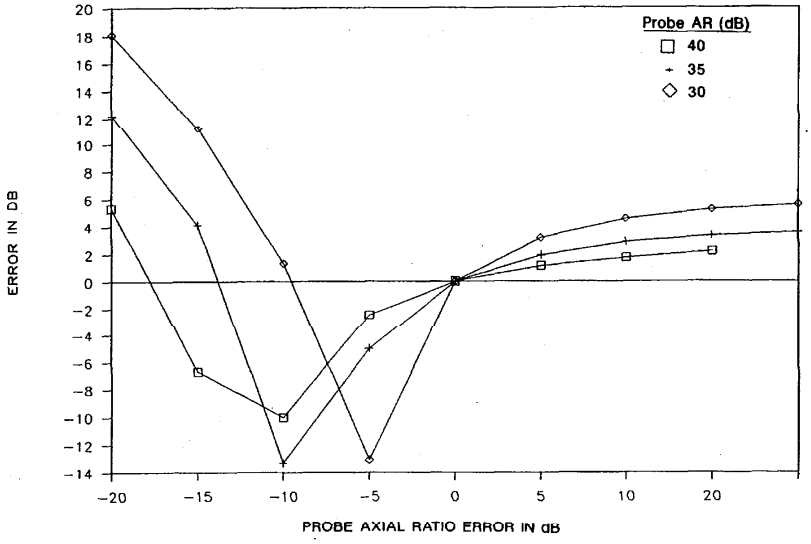

Fig. 2. Worst-case axial ratio error for linear polarization due to error in probe's polarization. AUT axial ratio is 30 dB.

The ratio of p's is then equivalent to axial ratio errors. In the first case, the complete probe correction is applied, but there is an error in ρ_s''. Fig. 2 shows the worst-case curves under the assumptions that

$$\arg\,(p_t(\mathbf{K})) \simeq -\pi/2 \tag{33a}$$

and

$$\arg\,(\rho_s''(\mathbf{K})) \approx \arg\,(\rho_{s\epsilon}''(\mathbf{K})) \approx \pi/2. \tag{33b}$$

These are consistent with the assumed field polarization, and for linear polarization it is generally the magnitude of $\rho_s''(\mathbf{K})$ that is in error, not its phase.

Next we consider the effect of assuming that both probes are perfectly polarized and therefore use only the principal component pattern of each probe in the probe correction. This is equivalent to assuming

$$\rho_s'(\mathbf{K}) = 0, \qquad \rho_{s\epsilon}''(\mathbf{K}) = \infty \tag{34}$$

and the error is now

$$\frac{p_{t\epsilon}(\mathbf{K})}{p_t(\mathbf{K})} \simeq 1 + \frac{1}{p_t(\mathbf{K})\rho_s''(\mathbf{K})}. \tag{35}$$

Fig. 3 shows the axial ratio errors to be expected for various AUT probe combinations under the assumptions of (33). From these and similar curves the need for, and accuracy of polarization probe correction for linear antennas can be determined.

Next we consider two cases of nominally circular polarization for the AUT and probes. The error equations corresponding to (32) and (35) are written in terms of axial ratios by

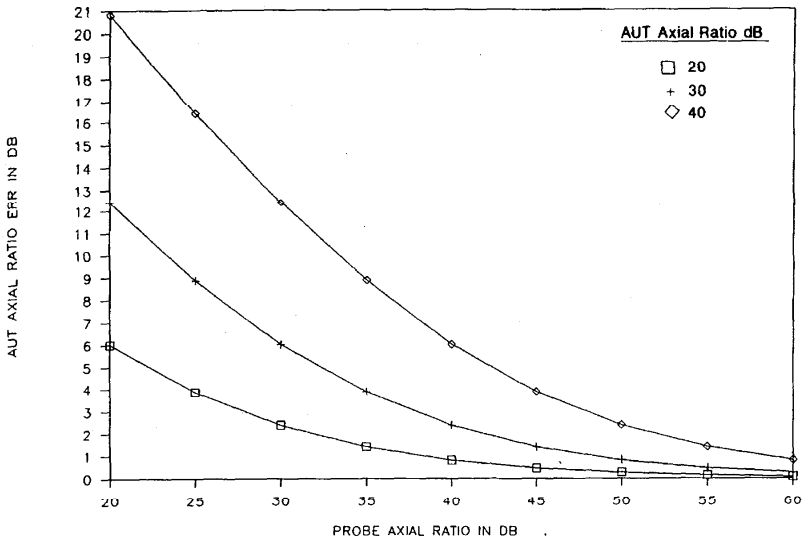

Fig. 3. Worst-case ratio error for linear polarization due to neglecting probe's polarization. AUT axial ratio is 30 dB.

noting from (14) that for small axial ratios in decibels,

$$\mathrm{AR}_t(\mathbf{K}) \simeq 17.3|p_t(\mathbf{K})| \text{ for right-circular} \tag{36a}$$

and

$$\mathrm{AR}_t(\mathbf{K}) \simeq 17.3|1/p_t(\mathbf{K})| \text{ for left-circular} \tag{36b}$$

with similar relations for the probes. Using these in (31) and noting that the AUT is right-circular while the cross-polarized probe is left-circular,

$$\begin{aligned}\Delta\mathrm{AR}_t(\mathbf{K}) &= \text{axial ratio error in dB} \\ &= |\mathrm{AR}_t(\mathbf{K})e^{i2\tau_t} + \mathrm{AR}_s''(\mathbf{K})e^{-i2\tau_s''} \\ &\quad - \mathrm{AR}_{s\epsilon}''(\mathbf{K})e^{-i2\tau_{s\epsilon}''}| - \mathrm{AR}_t(\mathbf{K}),\end{aligned} \tag{37}$$

where

τ_t tilt angle for the AUT,
τ_s'' correct tilt angle for the probe,
$\tau_{s\epsilon}''$ tilt angle used for the probe.

These tilt angles are less accurate than for linear polarization since they are for circularly polarized antennas. Fig. 4 shows plots of the AUT axial-ratio error as a function of probe axial-ratio error for $\tau_t = 0$ and various combinations of τ_s'' and $\tau_{s\epsilon}''$. From the figure and (37), the error is bounded by the extremes

$$\Delta\mathrm{AR}_t(\mathbf{K}) \leqslant \text{(probe axial ratio + axial ratio used)}. \tag{38}$$

This condition occurs only under the very special case when the actual and assumed probe polarization phases are 180° different *and* the AUT polarization phase is identical to one of these. More typical values are represented by the other curves. This is illustrated in Fig. 5 where the distribution of errors has been calculated for a uniform distribution of all possible phase conditions. The maximum occurs for less than one percent of the combinations, and the most probable values are in the region of the probes' axial ratio.

If the probe polarization is not used in the probe correction, this is equivalent to assuming that

$$\mathrm{AR}_{s\epsilon}''(\mathbf{K}) = 0 \tag{39}$$

and the error in this case is bounded again by the extreme and rare situation,

$$\Delta AR_t(\mathbf{K}) \leqslant \pm\text{probe axial ratio}. \tag{40}$$

The curve in Fig. 5 for no polarization correction shows the probable value again peaked at the probes' axial ratio value.

Probe alignment errors can be considered as a part of the probe pattern and polarization errors. The probe's receiving properties are measured or calculated with respect to a coordinate system fixed to the probe. When it is mounted for near-field measurements, errors in its alignment effectively rotate the coordinate system. Since the probe pattern is generally slowly varying, azimuth and elevation misalignments produce very small probe pattern errors. Rotation misalignments about the z axis produce errors in $\rho_s'(\mathbf{K})$ or $\rho_s''(\mathbf{K})$ which can be significant. These can be estimated using the probe polarization pattern, the rotation error, and (37) for the effect of probe polarization errors.

B. Near-Field Measurement Errors

Items 5–18 in Table I are the individual sources which contribute to errors in the spectra $D'(\mathbf{K})$ and $D''(\mathbf{K})$. These errors will be discussed in the order they appear in Table I. We will describe what effect they have on far-field results, summarize error equations, and describe what computer or experimental tests can be performed to quantify the errors.

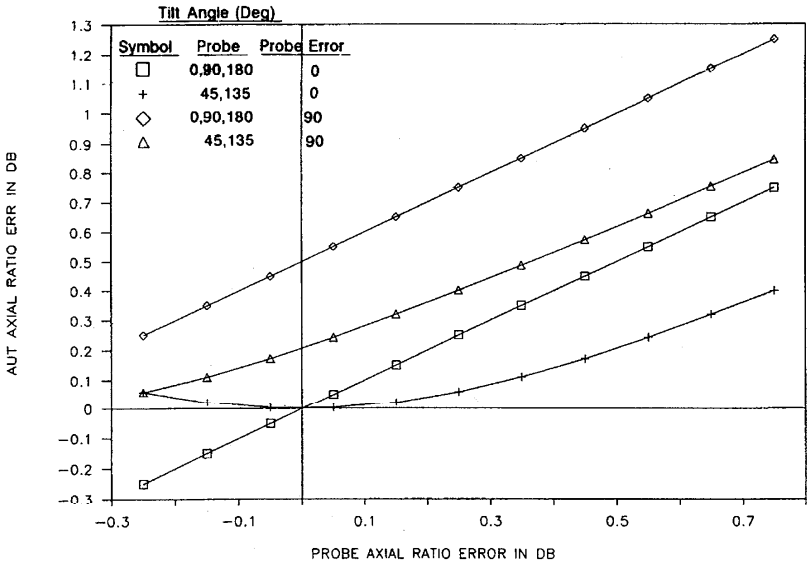

Fig. 4. Axial ratio error for circularly polarized antenna due to probe polarization errors for different probe tilt angles and tilt angle errors. AUT tilt angle is zero.

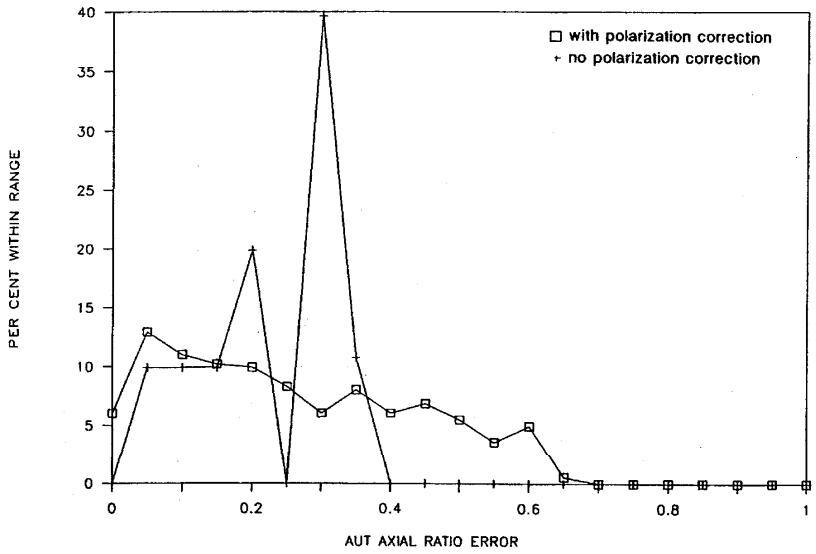

Fig. 5. Distribution of axial ratio errors for 0.5-dB axial ratio AUT due to errors in probe axial ratio and tilt angle.

The computer tests [2] use either actual or hypothetical near-field data to represent perfect error-free data. These data are then modified with errors of various types and magnitudes. Differences between far-field parameters computed from the error-free and modified data sets are a direct measure of the effect of each error source. The experimental tests are essentially a self-comparison technique where measurements on a given antenna are repeated after making a known, specific change in the system. Ideally, the change is made to produce a sign reversal in the effect of only one error, and the difference between the two measurements is then a direct measure of that specific error. In the equations of this section, single or double primes on $B(\mathbf{P})$, $D(\mathbf{K})$, and the normalization constant A will be dropped since the relations refer to either case.

Gain Errors

We first consider those error sources which produce a constant effect on the far-field pattern; that is, they are

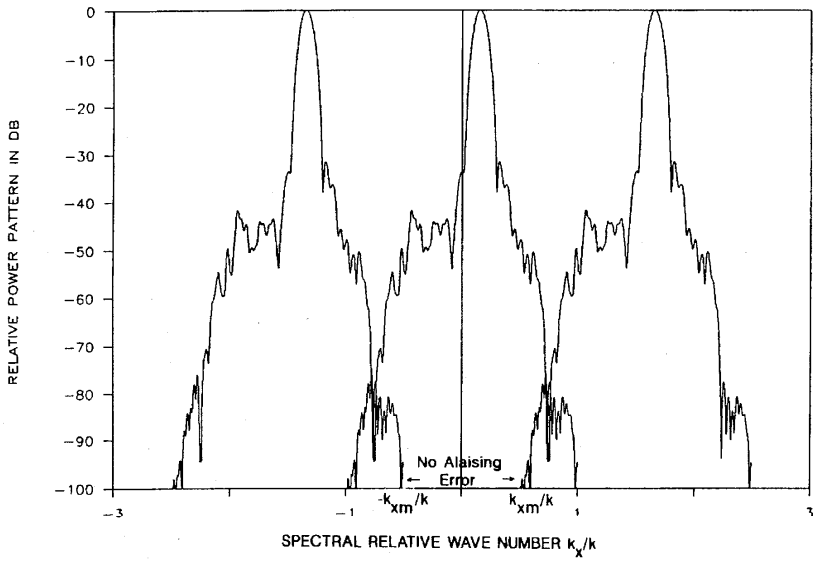

Fig. 6. Illustration of aliasing error due to overlapping of offset spectra.

generally not functions of **K**. These errors affect only the peak gain and other related power parameters. Using a concise version of the gain equation [3] for near-field measurements, we obtain

$$\frac{\Delta G_m(K_0)}{G_m(K_0)} = \frac{\Delta M}{M} + \frac{\Delta|\Sigma B_0(\mathbf{P})e^{-i\mathbf{K}_0\cdot\mathbf{P}}|^2}{|\Sigma B_0(\mathbf{P})e^{-i\mathbf{K}_0\cdot\mathbf{P}}|^2} - \frac{\Delta G_p(\mathbf{K}_0)}{G_p(\mathbf{K}_0)} - \frac{\Delta|A_n|^2}{|A_n|^2} \tag{41}$$

where ΔM and M refer to the impedance mismatch factor and the Δ's in each case denote the errors in the quantities.

Alignment Errors: Antenna alignment errors imply that the antenna coordinate system as defined by mirrors, fiducial marks, tooling balls, or a boresight scope is not precisely aligned with that of the mechanical scanner. Since pattern results are defined with respect to the mechanical scan plane, angular misalignment of the AUT will produce boresight errors equal to the azimuthal and elevation rotation errors. Small misalignment about the z axis will produce approximately equivalent errors in the tilt angle for **K** values not too far off axis.

Aliasing Errors: In principle, data point spacings can be chosen so that aliasing errors are arbitrarily small, but noise and rapidly varying systematic errors set the practical lower limit. As developed in the theory [1], [4], the summation of incremental data going from the integral of (5) and (6) to the digital Fourier transform (DFT) is exact (there is no aliasing error) if the Fourier transform of the measured data is band-limited with band limits k_1 and k_2, and the data point spacings satisfy the sampling criteria

$$\delta_x \leqslant \frac{\pi}{k_1} \qquad \delta_y \leqslant \frac{\pi}{k_2}, \tag{42}$$

corresponding to those band limits. If band limits do not exist, or if the sampling criteria are violated by using larger data point spacings, aliasing errors occur in the use of the FFT to calculate the Fourier transform. The character of these errors can be illustrated by considering the near-field data $B(\mathbf{P})$ sampled at intervals δ_x, δ_y. Let us denote the true spectrum of $B(\mathbf{P})$ and its DFT as calculated by summation as $F(\mathbf{K})$ and $F_e(\mathbf{K})$, respectively. The term "true spectrum" as used here means the Fourier transform of the actual measured data excluding any aliasing errors. Since the data include the effects of measurement errors as well as spectral properties of the probe and AUT, the true spectrum is composed of two parts.

$$F(\mathbf{K}) = D(\mathbf{K})e^{i\gamma d} + \epsilon(\mathbf{K}), \tag{43}$$

the first term corresponding to the coupling product of probe and AUT spectra, and the second arising from noise and other sources of error in the measured data. As illustrated in Fig. 6 and (44), the calculated spectrum is the sum of offset replicates of the true spectrum which overlap at $(2m-1)k_1$, and $(2n-1)k_2$ [5]

$$\begin{aligned} F_e(\mathbf{K}) &= \sum_{m,n=-\infty}^{\infty} F(k_x+2mk_1,\ k_y+2nk_2) \\ &= \sum_{m,n=-\infty}^{\infty} D(k_x+2mk_1,\ k_y+2nk_2)e^{i\gamma_{m,n}d} \\ &\quad + \epsilon(k_x+2mk_1,\ k_y+2nk_2) \end{aligned} \tag{44}$$

where

$$\gamma_{m,n} = \sqrt{k^2-(k_x\pm 2mk_1)^2-(k_y\pm 2nk_2)^2}. \tag{45}$$

The aliasing error is due to the contributions of the terms for

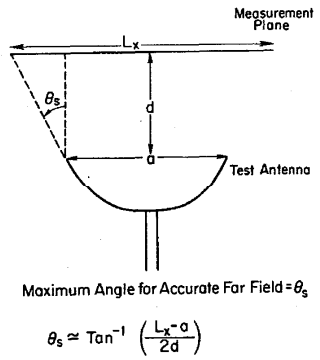

Fig. 7. Relationship between scan length and angular region of validity.

$m \neq 0$, $n \neq 0$, within the region $|k_x| \leqslant k_1$, $|k_y| \leqslant k_2$. The aliasing error from the terms involving the factor $e^{i\gamma_{m,n}d}$ can be made arbitrarily small by making δ_x and δ_y small enough; the terms involving the error spectrum are, therefore, the limiting lower bound. In most cases, only the terms for $m = n = \pm 1$ will make a significant error contribution, and from estimates of $D(\mathbf{K})$ arrived at from either measured or theoretical probe and AUT patterns, the bound of the resulting aliasing errors can be reliably determined.

In some cases, pattern results for a narrow-beam antenna may be required only over a limited region centered on $\mathbf{K} = 0$. The data point spacings may then be increased beyond the value specified by the sampling criteria, producing aliasing errors outside the region of interest while limiting the errors within. For example, if the region of interest is bounded by

$$|k_y| \leqslant k_{ym} \qquad |k_x| \leqslant k_{xm}, \tag{46}$$

only evanescent spectra will overlap this region if

$$\delta_x \leqslant \frac{\lambda}{(1 + k_{xm}/k)} \qquad \delta_y \leqslant \frac{\lambda}{(1 + k_{ym}/k)}. \tag{47}$$

as illustrated in Fig. 6. Measurement and data processing time can, therefore, be reduced by using the larger spacings with little change in accuracy with the region of interest.

To estimate the error due to aliasing, $F(\mathbf{K})$ or its two parts, $D(\mathbf{K})e^{i\gamma d}$ and $\epsilon(\mathbf{K})$, must be measured or estimated. This can often be accomplished with either centerline near-field data tests or theoretical antenna patterns along with measurements of system noise and error levels.

Truncation Errors: The area truncation has two effects. First, for areas larger than the aperture the pattern results are valid only within the angular region defined by the geometry of the antenna and the scan area, as shown in Fig. 7. This result has been developed empirically from extensive measurements [6] and derived from a theoretical analysis [7]. It may be surprising that a simple relation is valid for such a complicated situation, but it has been validated for a large number of antenna and probe combinations. This criterion is used to determine the minimum size of the scan plane for a given desired angular region of coverage and separation distance d. Since the lower limit on d is set by the physical structure of the antenna and multiple reflections, a trade-off is usually necessary between either maximizing angular coverage along with reducing truncation errors or minimizing multiple reflection errors.

The second effect of area trunction produces some errors in $D(\mathbf{K})$ even within the "region of validity" shown in Fig. 7. Yaghjian [7] showed that this error can be estimated from a knowledge of the measured data on the boundary of the scan area, even though the error results from neglecting all the data on the infinite plane outside the scan area. If we denote the plane polar coordinates of the boundary as (p', ϕ_p), the data on the boundary as $B(p', \phi_p)$, and the spherical coordinates of the far-field directions by (θ, ϕ), then the fractional error in that direction is

$$\frac{|\Delta D(\theta, \phi)|}{|D(\theta, \phi)|} \leqslant \lambda \frac{\left|\int_0^{2\pi} B(p', \phi_p)^{-ikp' \sin\theta \cos(\phi - \phi_p)} p' \, d\phi_p\right|}{2\pi\delta_x\delta_y \cos\gamma_{\max} |\Sigma B(p', \phi_p) e^{-i\mathbf{K}\cdot\mathbf{P}}|} \tag{48}$$

where $\gamma_{\max}$ is the maximum acute angle between the plane of the scan area and any line connecting the edges of the antenna aperture and the scan area. Equation (48) can be easily evaluated after measurements have been completed and $B(P', \phi_p)$ is known. If preliminary estimates of the truncation error are desired, another relation is available requiring less information, but generally predicting much larger upper bound errors; specifically,

$$\frac{|\Delta D(\mathbf{K})|}{|D(\mathbf{K})|} \leqslant \frac{\alpha\lambda L^{\max} B_{\max}(p', \phi_p)}{2A \cos\gamma_{\max}} g(\mathbf{K}) \tag{49}$$

where

A area of antenna aperture,
$L^{\max}$ maximum width of scan area,
α $\approx 1 - 5$, taper factor (see discussion by Yaghjian in [6])
$g(\mathbf{K})$ $= |D(\mathbf{K}_0)/D(\mathbf{K})|$, ratio of peak pattern amplitude at $\mathbf{K}_0$ to the amplitude at $\mathbf{K}$.

The character of the truncation error can be seen clearly from the plot in Fig. 8 of the magnitude of $D(\mathbf{K})$ for the single direction $\mathbf{K} = 0$ as a function of the data area used in the summation of (5b). Each point on the curve represents a calculated value of $D(0)$ for increasing areas, starting in the center of the data array. Another way of estimating the effect of truncation involves the use of (48) and the actual measured data to calculate an effective "error spectrum" resulting from the finite scan area. This error spectrum is obtained by calculating the Fourier transform of the measured data with all measured amplitudes not on the boundary set to zero. This spectrum is basically the numerator of (48) and represents an upper bound estimate of the error spectrum produced by truncation. An example of this test is shown in Fig. 9.

Position, Multiple Reflection, and Receiver Errors: For the sources of errors thus far considered, reliable and

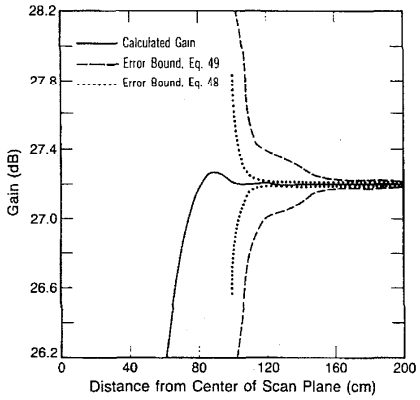

Fig. 8. Calculated gain versus scan ara radius showing effect of truncation error.

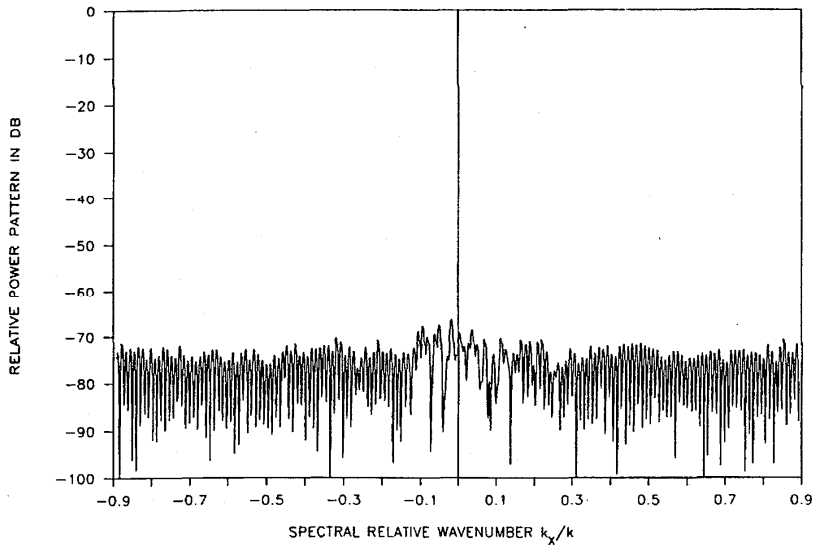

Fig. 9. Error spectrum relative to beam peak due to area truncation.

reasonable estimates of their effect have been obtained without the need for much additional information beyond the normal data, $B(\mathbf{P})$, A, and the probe parameters $s_{02}(\mathbf{K})$. For the remaining errors, probe position errors, multiple reflections, and system amplitude or phase nonlinearities, either more information is required or the error bounds will be unrealistically large. Equations have been derived [6] for the latter group that give the upper bound effects in terms of the *maximum* value of the near-field error and pertinent antenna parameters. In the sidelobe region, a common assumption implicit in the derivation of each of these equations is that the variation of the error as a function of probe position $\mathbf{P}$ is such that it concentrates its maximum effect in the direction of observation. In most cases, this is a sinusoidal error. For instance, if the z-position error is of the form

$$\Delta z(x, y) = \delta_{z\,\max} \cos\left(\frac{2\pi x}{\tau_x}\right) \tag{50}$$

and the main beam is along the z axis, the sidelobes in the directions

$$\frac{k_x}{k} = \pm\frac{\lambda}{\tau_x} = \sin AZ \tag{51}$$

will be in error by the amount predicted by the upper bound equations, but in all other directions, the error will be essentially zero. If only $\delta_{z\,\max}$ is known, we must either conclude that any sidelobe could be in error by the upper

bound value or make some estimate based on the probability of the distribution over all values of **K**. A more realistic estimate can be made if the actual error function is known, say from optical or mechanical measurements on the mechanical probe x–y scanner. From actual measured values of $\Delta z(x, y)$, the Fourier components may be calculated for each direction yielding

$$\delta_z(\mathbf{K}) = \frac{1}{4\pi^2} \int \Delta z(x, y) e^{-i\mathbf{K}\cdot\mathbf{P}}\, d\mathbf{P}. \tag{52}$$

The far-field error in any direction is given by the upper bound equations with $\delta_z(\mathbf{K})$ as the magnitude of the near-field error rather than the maximum value $\delta_{z\,\max}$.

This concept is also valid for the equations related to multiple reflection, x–y position, and system nonlinear response errors. Therefore, in the following equations for errors in the sidelobe region, the parameters denoting the magnitude of the near-field errors will appear as functions of **K**. These parameters may then be interpreted in one of two ways. 1) Lacking information about the spatial (x, y) dependence of the error, the parameter is a constant equal to its maximum value. The resulting error estimates will predict a worst-case error in every far-field direction. 2) If data are available to specify the spatial dependence of the error, the magnitude parameter is the result of a Fourier decomposition on the near-field error data and the error equations will predict upper bound errors nearly equal to the actual errors for every direction. The latter option is preferable where possible, and in the following, techniques will be described to obtain the spatial dependences of the error functions.

The error functions producing the maximum effect are different in the main beam region than for sidelobes. Constant and long period types are predominant; however, for z-position errors, even random errors with the same rms value as a systematic error will have the same effect on the gain. The same is true for x, y-position errors when the main beam is steered off the z axis. These facts are reflected in (56) and (59), where the rms subscript indicates that this value rather than the spectral magnitude is used.

The equations below are derived for the case of directional antennas where the antenna's maximum dimension is on the order of 5–10λ or greater. Since the planar technique is generally used for such antennas, this is the most important case. For electrically small antennas, similar equations may be derived from the basic analysis presented in the references.

For the following equations, the following notations will be used:

$D(\mathbf{K})$	true plane-wave spectrum for a sum pattern,
$\tilde{D}(\mathbf{K})$	true plane-wave spectrum for a difference pattern,
$\tilde{D}(\mathbf{K}_m)$	maximum value of difference pattern,
$\mathbf{K}_b$	value of **K** for the boresight direction of a beam steered off-axis,
θ_b	polar angle between the z axis and the boresight direction of main beam or difference null,
θ	polar angle between $\mathbf{K}_b$ and **K**,
$D_e(\mathbf{K})$, $\tilde{D}_e(\mathbf{K})$	spectra determined from actual near-field data for sum and difference patterns containing errors due to some single type of near-field error such as probe position error, multiple reflections, etc.,
η	antenna aperture efficiency,
Q	difference in dB between the two maxima of a far-field difference pattern,
L	maximum antenna dimension,
$\Delta(\mathbf{K})$	spectrum of the near-field x- or y-position errors, $\Delta_x(x, y)$, $\Delta_y(x, y)$.
$\delta_z(\mathbf{K})$	spectrum of the near-field z-position error $\delta_z(x, y)$,
$g(\mathbf{K})$	$= \lvert D(\mathbf{K}_b)/D(\mathbf{K})\rvert$ or $\lvert\tilde{D}(\mathbf{K}_m)/\tilde{D}(\mathbf{K})\rvert$, ratio of pattern maximum to amplitude in the direction under consideration,
K	direction in which the error is being determined.

Using the above notation, the errors in the spectra due to near-field x, y-position errors are as follows.

a) If the antenna boresight is along the z axis and **K** denotes directions close to boresight where $\theta < \lambda/10L$,

$$\left|\frac{D_e(\mathbf{K})}{D(\mathbf{K})}\right|_{\mathrm{dB}} \leqslant \frac{8.7\Delta(\mathbf{K})}{\eta L}\, g(\mathbf{K}) \tag{53}$$

$$\left|\frac{\tilde{D}_e(\mathbf{K})}{\tilde{D}(\mathbf{K})}\right|_{\mathrm{dB}} \leqslant \frac{8.7\Delta(\mathbf{K})}{\eta L}\, g(\mathbf{K}). \tag{54}$$

b) If the antenna boresight is along the z axis and **K** denotes directions away from boresight where $\lambda/10L < \theta < \pi/2$,

$$\left|\frac{D_e(\mathbf{K})}{D(\mathbf{K})}\right|_{\mathrm{dB}} \approx \left|\frac{\tilde{D}_e(\mathbf{K})}{D(\mathbf{K})}\right| \leqslant \frac{4.3\Delta(\mathbf{K})}{L}\, g(\mathbf{K}). \tag{55}$$

c) If the antenna's main beam is steered off the z axis and **K** denotes directions near boresight,

$$\left|\frac{D_e(\mathbf{K}_b)}{D(\mathbf{K}_b)}\right|_{\mathrm{dB}} \leqslant \frac{344}{\sqrt{\eta}} \left(\frac{\Delta\mathrm{rms}}{\lambda}\right)^2 \sin^2\theta_b g(\mathbf{K}) \tag{56}$$

$$\left|\frac{\tilde{D}_e(\mathbf{K}_b)}{\tilde{D}(\mathbf{K}_b)}\right|_{\mathrm{dB}} \leqslant \frac{3Q\Delta(\mathbf{K})}{\lambda} \sin\theta_b g(\mathbf{K}). \tag{57}$$

d) If the antenna's main beam is steered off the z axis and **K** denotes directions away from boresight,

$$\left|\frac{D_e(\mathbf{K})}{D(\mathbf{K})}\right|_{\mathrm{dB}} \approx \left|\frac{\tilde{D}_e(\mathbf{K})}{\tilde{D}(\mathbf{K})}\right| \leqslant \frac{13.5\Delta(\mathbf{K})}{\lambda} \sin\theta_b g(\mathbf{K}). \tag{58}$$

The errors in the spectra near the main beam due to z-position errors are

$$\left|\frac{D_e(\mathbf{K})}{D(\mathbf{K})}\right|_{\mathrm{dB}} \leqslant \frac{43}{\sqrt{\eta}} \left(\frac{\delta_z\mathrm{rms}}{\lambda}\right)^2 \cos^2\theta_b g(\mathbf{K}) \tag{59}$$

$$\left|\frac{\tilde{D}_e(\mathbf{K})}{\tilde{D}(\mathbf{K})}\right|_{\mathrm{dB}} \leqslant \frac{3.4Q\delta_z(\mathbf{K})}{\lambda} \cos\theta_b g(\mathbf{K}). \tag{60}$$

In the sidelobe region,

$$\left|\frac{D_e(\mathbf{K})}{D(\mathbf{K})}\right|_{\text{dB}} \approx \left|\frac{\tilde{D}_e(\mathbf{K})}{\tilde{D}(\mathbf{K})}\right|_{\text{dB}} \leqslant \frac{13.5\delta_z(\mathbf{K})}{\lambda} \cos\theta_b g(\mathbf{K}). \quad (61)$$

Equations (59)–(61) apply to both steered and nonsteered beams.

The position error functions, $\delta_z(x, y)$, $\Delta_x(x, y)$, and $\Delta_y(x, y)$ can be measured very accurately with a laser interferometer. If the mechanical system is stable, such a measurement is required when the system is originally installed and then only at periodic intervals to guarantee accuracy.

The effect of the multiple reflections on the measured data can be seen clearly from plots similar to Fig. 10. The probe has been placed at a fixed x, y-position and the separation distance varied. The periodic variations with peak-to-peak magnitudes denoted by w shown in Fig. 10 are due to the multiple scattering between the probe and test antenna. The analysis [6] shows that the error in any direction could be as large as

$$\left|\frac{D_e(\mathbf{K})}{D(\mathbf{K})}\right|_{\text{dB}} \leqslant \frac{w}{2} g(\mathbf{K}) \quad (62)$$

where w is in decibels.

This predicts very large errors in the sidelobe region, and the actual error will depend on the variation of w in both amplitude and phase as a function of position. In this case, the technique used to measure $w(\mathbf{P})$ can also measure the error directly and, therefore, reduce or eliminate it. This is accomplished by measuring the near-field data at a series (2)–(5) of closely spaced planes over a z distance of $\lambda/2$. The average of the results tends to remove the effect of multiple reflections and the difference between the average and any individual results gives the error. This approach requires much extra data and is generally done only to achieve the highest accuracy, or at one of a series of frequencies, to establish reliable error estimates. The measurement effort can also be reduced by using centerline data instead of full scans to estimate error bounds.

Amplitude and phase instrumentation errors arise from receiver nonlinearity, flexing of the cable connected to the probe, and drift. All of these combine to produce the measured amplitude $a_e(\mathbf{P})$ rather than the true amplitude $a(\mathbf{P})$. The receiver amplitude error is modeled with a nonlinearity function, $\mu(\mathbf{P})$,

$$a_e(\mathbf{P}) = (1 + (a_e(\mathbf{P}) - 1)\mu(\mathbf{P}))a(\mathbf{P}). \quad (63)$$

The contribution to μ from the receiver nonlinearity can be measured and partially corrected for by calibrating the receiver with a precision variable attenuation. The same is also true of the other contributors to amplitude error and, in estimating final errors, the corrected value of $\mu(\mathbf{P})$ should be used. If we denote the Fourier transform of $\mu(\mathbf{P})$ by $U(\mathbf{P})$, the resulting error is

$$\left|\frac{D_e(\mathbf{K})}{D(\mathbf{K})}\right|_{\text{dB}} \leqslant 6U(\mathbf{K})g(\mathbf{K}). \quad (64)$$

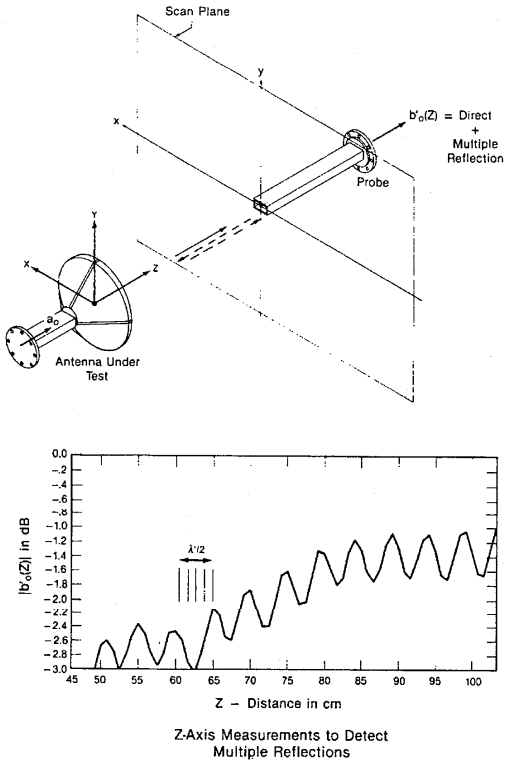

Fig. 10. Multiple reflection between AUT and probe indicated by periodic variations with $\lambda/2$ period.

Instrumentation phase errors arise from the same sources as amplitude errors and can be treated in much the same manner. If we denote the residual, uncorrected phase errors as $\Delta\psi(\mathbf{P})$ and the corresponding transform by $V(\mathbf{K})$, the effect on $D(\mathbf{K})$ is very similar to z-position errors, and

$$\left|\frac{D_e(\mathbf{K})}{D(\mathbf{K})}\right|_{\text{dB}} \leqslant \frac{43}{\sqrt{\eta}} \left(\frac{\Delta\psi\text{rms}}{360}\right)^2 g(\mathbf{K}) \quad (65)$$

$$\left|\frac{\tilde{D}_e(\mathbf{K})}{\tilde{D}(\mathbf{K})}\right|_{\text{dB}} \leqslant 3.4Q \frac{V(\mathbf{K})}{360} g(\mathbf{K}) \quad (66)$$

for $\theta < \lambda/10L$, and

$$\left|\frac{D_e(\mathbf{K})}{D(\mathbf{K})}\right|_{\text{dB}} \approx \left|\frac{\tilde{D}_e(\mathbf{K})}{\tilde{D}(\mathbf{K})}\right|_{\text{dB}} \leqslant 13.5 \frac{V(\mathbf{K})}{360} g(\mathbf{K}) \quad (67)$$

when $\lambda/10L \leqslant \theta \leqslant \pi/2$.

Dynamic Range: Since the effect of limited dynamic range is so dependent on the receiver characteristics and the near-field pattern, measurement tests are the best method for estimating the resulting errors. Computer simulation can be used where the amplitude data are artifically set to zero at various levels. The more serious effect is generally on the phase, however, and it is difficult to predict how the phase errors will be influenced by different dynamic ranges. One

characteristic that is typically observed with phase/amplitude receivers is where the phase readings tend to become constant as the amplitude is reduced below some level. This has a very serious effect on the far-field pattern, since under Fourier transform these measurements are erroneously applied to the main beam region instead of the sidelobes. Both regions are then in error.

Tests for receiver dynamic range are of two types. In the first, the probe is placed at a fixed position, or to increase available signal levels, the generator and load ports are connected directly together. The input signal is then decreased in steps while noting both the amplitude and phase response. The upper limit for receiver signal is determined by linear amplitude response as indicated when the amplitude reading change for a given step remains constant for input signal variation. The lower level is indicated when the phase readings begin to change by more than 5°–10° from their initial value. This defines the receiver's dynamic range, but it does not determine what effect it will have on the far-field results. For this a second set of tests is required. A series of near-field data sets is taken with decreasing levels of input signal to the AUT. Comparing the far-field results for the different signal levels quantifies the effect of reduced dynamic range. These tests can be time-consuming if two-dimensional data are used, and in many cases one-dimensional centerline scans are adequate.

Room Scattering: Scattering by fixed objects in the room is not generally detected by the probe/antenna multiple reflection test. Room scattering is best observed if the AUT and probe are moved together relative to the room. Scattered signals then go in and out of phase with the direct signal, and this variation is a direct measure of the level of scattering. In one application of this approach, the test antenna was mounted on a set of accurately aligned rails parallel to the scanner's x axis so that it could be moved in the x direction without changing its angular alignment or its y or z positions relative to the probe. In the antenna's initial position, the probe was moved in the y direction, and amplitude and phase data were recorded. The probe and antenna were then moved in the x direction by the same increment and the y scan repeated. This process was repeated for an x movement over the complete scan distance. The measured data were analyzed to detect differences due to scattering, and the largest such signals were at least 40 dB below the peak direct signal. In the far field, the uncorrelated nature of the scattering reduced its effect to a spectrum approximately 70 dB below the main beam.

Leakage: Leakage and crosstalk occur when transmission lines on either the transmitting or receiving side radiate or receive RF energy, or when signals within the receiver's reference and measurement channels interfere. An effective test for leakage is accomplished by terminating the generator port and measuring the signal picked up by the probe as compared to the direct signal. A sample of such a test is shown in Fig. 11. In this example, a faulty cable caused the observed increase in signal in one region. A similar test of leakage on the receiver side is accomplished by substituting a termination in place of the probe and repeating the scan. The leakage and crosstalk have the biggest effect when measuring antenna with

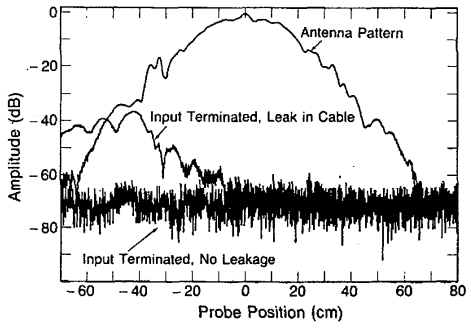

Fig. 11. Leakage measurement with generator port terminated.

gains less than about 30 dB. The error signal tends to have a relatively constant phase over the scan area, and adds up to a significant level in the Fourier transform. Because the sum of the measured relative data is approximately equal to the effective area of the AUT,

$$A_e \approx \sum_{i=1}^{N} B(\mathbf{P}_i) e^{-i\mathbf{K}_0 \cdot \mathbf{P}_i} \delta_x \delta_y \tag{68}$$

and

$$\sum_{i=1}^{N} B_c(\mathbf{P}_i) e^{-i\mathbf{K}_0 \cdot \mathbf{P}_i} \delta_x \delta_y \approx N B_c \delta_x \delta_y. \tag{69}$$

The ratio of peak antenna gain to leakage signal gain is

$$\frac{G_a}{G_c} \approx \frac{A_e}{A_m B_c} \tag{70}$$

where

G_c leakage signal gain,
A_m measurement area,
B_c leakage signal relative to peak measurement signal.

The error in AUT gain is then given by

$$\Delta G_a \approx \frac{4.3 A_m B_c}{A_e}. \tag{71}$$

For high gain antennas, the ratio of measurement area to effective area is only about 4:1, but for lower gain antennas it can be as high as 100:1 and even though B_c may be 60 dB below the measurement signal, gain errors of 0.4 dB can occur. One test to measure the actual effect of these errors is to record a complete two-dimensional scan with either the generator or load ports terminated. Transformation of these data will then quantify the actual error spectrum. As with other tests like this, they are usually done on a representative frequency/beam/polarization/port combination.

Random Errors: The last error source is the net random error in amplitude and phase due to mechanisms in the mechanical and electrical system. Mathematical analysis [8] has developed expressions for the far-field signal-to-noise

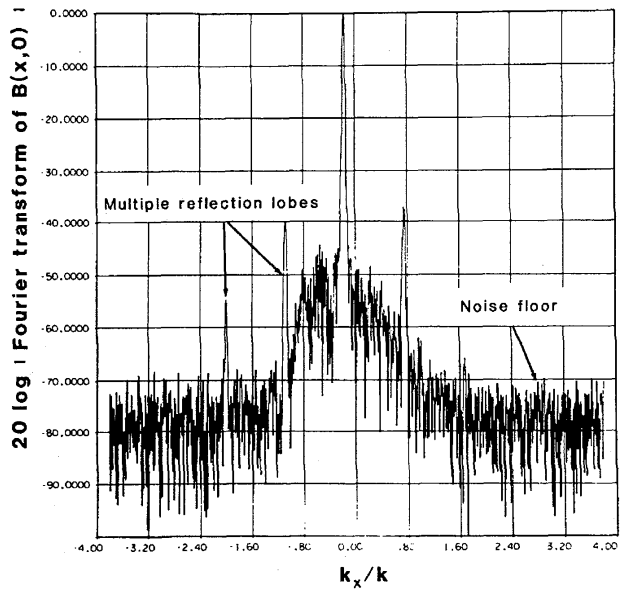

Fig. 12. Spectrum resulting from measurements at data point spacings less than $\lambda/2$ showing noise spectrum and multiple reflection lobes in region where $|k_x|^k$.

ratio in the sidelobe region due to random amplitude errors:

$$\left|\frac{D(\mathbf{K}_0)}{\epsilon_a(\mathbf{K})}\right| \geq \frac{\sqrt{N}A_a\eta}{3\sqrt{2}A_m\sigma_a} = \frac{\sqrt{N_e/2}}{3\sigma_a\sqrt{N/N_e}} \tag{72}$$

where

N total number of measurement points,
N_e $A_e/\delta_x\delta_y$, number of measurement points within the effective area,
A_a actual area of AUT,
$A_m \simeq N\,\delta_x\delta_y$,
σ_a standard deviation of random amplitude errors.

A similar expression for the phase error is

$$\left|\frac{D(\mathbf{K}_0)}{\epsilon_\psi(\mathbf{K})}\right| \geq \frac{\sqrt{Ne/2}}{3\sigma_\psi}. \tag{73}$$

Computer simulation has been used to verify the essential features of (72) and (73). In these tests, actual data were assumed to represent error-free measurements from which the correct spectrum could be calculated. Random amplitude and/or phase errors with known distributions were then added to the original data and such quantities as $\epsilon_a(\mathbf{K})$, $\epsilon_\psi(\mathbf{K})$, and the signal-to-noise ratios directly calculated.

To use (72) and (73), the standard deviations of the random amplitude and phase distributions are required. These can be obtained by measuring or estimating the contributions of such sources as resolution in analog-to-digital converters, receiver noise, scattering within the room, random position errors, etc. An alternate method makes use of near-field centerline data. These data are taken at spacings much less than $\lambda/2$ and allow calculation of the spectrum for values of either k_x/k or k_y/k beyond ± 1 as shown in Fig. 12. These data were taken at a z spacing of about 6λ where actual evanescent modes are attenuated to such a low level they could not be detected. The calculated spectrum in the evanescent region therefore represents the effect of errors in the measurement, and the relatively constant floor level in this region is a direct observation of the effect of random errors in the measured data. From this direct measure of the signal-to-noise ratio in the one-dimensional (1D) spectrum the corresponding signal-to-noise for the two-dimensional (2D) data may be inferred. For instance, let the 1D measurement be taken in the x direction over a length l_x' with data point spacings δ_x'. The corresponding 2D data will involve data point spacings δ_x, δ_y and scan lengths l_x and l_y. The signal-to-noise ratio for the 2D measurement will then be

$$\left|\frac{D(\mathbf{K}_0)}{\epsilon(\mathbf{K})}\right|_{2D} = \left|\frac{D(\mathbf{K}_0)}{\epsilon(\mathbf{K})}\right|_{1D} \frac{l_x l_y \delta_x'}{l_x' \delta_y \delta_x}. \tag{74}$$

C. Combination of Errors

The problem of combining systematic and random errors to provide an overall estimate of accuracy has evoked heated discussion, and various viewpoints have evolved concerning this topic. Choosing the correct method for combining the systematic errors requires some knowledge about their error distribution. This information is not normally available from experimental tests and, at best, is obtained through an educated guess. We do know that to a first approximation the systematic errors are independent. Our viewpoint is that the method of combination assumes secondary importance if the estimates for each error source are tabulated and the formula used in the combined estimate is explicitly stated.

TABLE II
ERROR BUDGET FOR PEAK GAIN MEASUREMENTS

Error Source	Error (dB)
Probe relative pattern	0.00
Probe polarization ratio	0.00
Probe gain	0.10
Probe alignment	0.02
Normalization constant (or power measurement)	0.10
Impedance mismatch	0.05
AUT alignment	0.00
Aliasing error	0.00
Measurement area truncation	0.05
Probe x-y-position error	0.01
Probe z-position error	0.01
Multiple reflections	0.15
Receiver amplitude nonlinearity	0.01
System phase errors	0.00
Receiver dynamic range	0.02
Room scattering	0.05
Leakage and crosstalk	0.05
Random errors in amplitude and phase	0.00
RSS combination (dB)	0.23

TABLE III
ERROR BUDGET FOR -30 dB SIDELOBE MEASUREMENT

Error Source	Error (dB)
Probe relative pattern	0.10
Probe polarization ratio	0.05
Probe gain	0.00
Probe alignment	0.20
Normalization constant (or power measurement)	0.00
Impedance mismatch	0.00
AUT alignment	0.00
Aliasing error	0.05
Measurement area truncation	0.15
Probe x-y-position error	0.06
Probe z-position error	0.21
Multiple reflections	0.30
Receiver amplitude nonlinearity	0.07
System phase errors	0.23
Receiver dynamic range	0.20
Room scattering	0.05
Leakage and crosstalk	0.05
Random errors in amplitude and phase	0.00
RSS combination (dB)	0.53

The method we have adopted assumes that the component systematic uncertainties (ϵ_i) are independent and normally distributed with ϵ_i corresponding to 3σ. Because of the central limit theorem, the combined probability distribution will approach a Gaussian and we estimate the total error by

$$\epsilon_T = \sqrt{3\sigma_R^2 + \sum_i \epsilon_i^2}, \tag{75}$$

where ϵ_T represents the total error, ϵ_i the estimates of the worst-case systematic components, and σ_R is the standard deviation of the random component. Tables II and III, are typical results using the error equations and tests to determine each of the individual errors and then combining them using (75).

III. Summary

A combination of techniques has been described for reliably estimating the magnitude of each error arising in planar near-field measurements. They include mathematical analysis, computer simulation, and measurement tests. There are three primary applications for these tests. 1) In designing a new measurement facility, the requirements of each part of the measurement system can be specified in order to meet a given level of accuracy. 2) During actual measurements the experimentalist can identify, and reduce where necessary, potential sources of error in the measurement. 3) When a measurement has been completed, the estimated uncertainty in the measurement can be obtained with confidence and ease. The latter application has been used in many measurements to verify that the planar near-field technique produces high accuracy results competitive with any other measurement technique.

Acknowledgment

The author is extremely grateful to Arthur D. Yaghjian who developed much of the mathematical analysis, and who helped to formulate concepts through countless discussions. Carl F. Stubenrauch, Andrew G. Repjar, Michael H. Francis, and Douglas P. Kremer also have made major contributions through numerous measurement programs where the techniques have been developed and tested.

References

[1] D. M. Kerns, *Plane-Wave Scattering-Matrix Theory of Antennas and Antenna-Antenna Interactions.* Nat. Bur. Stand. Monograph 162, June 1981.

[2] G. P. Rodrigue, E. B. Joy, and C. P. Burns, "An investigation of the accuracy of far-field radiation patterns determined from near-field measurements," U.S. Army Missile Command, Redstone Arsenal, AL, Int. Rep., Aug. 1973.

[3] A. C. Newell, R. D. Ward, and E. J. McFarlane, "Gain and power parameter measurements using planar near-field techniques," *IEEE Trans. Antennas Propagat.*, pp. 792–803, this issue.

[4] E. B. Joy and D. T. Paris, "Special sampling and filtering in near-field measurements," *IEEE Trans. Antennas Propagat.*, vol. AP-20, pp. 253–261, May 1972.

[5] A. V. Oppenheim and R. W. Shafer, *Digital Signal Processing.* Englewood Cliffs, NJ: Prentice-Hall, 1975. pp. 115–121.

[6] A. D. Yaghjian, "Upper-bound errors in far-field antenna parameters determined from planar near-field measurements, Part 1: Analysis," Nat. Bur. Stand., and Tech. Note 667, 1975.

[7] A. C. Newell and M. L. Crawford, "Planar near-field measurements on high performance array antennas," Nat. Bur. Stand., NBSIR 74-380, July 1974.

[8] A. C. Newell and C. F. Stubenrauch, "Effect of random errors in planar near-field measurements," *IEEE Trans. Antennas Propagat.*, pp. 769–773, this issue.

Allen C. Newell (M'73–M'81–SM'83), for a photograph and biography please see page 733 of this issue.